Universidad Carlos III de Madrid
e-Archivo

Institutional Repository

This document is published in:

Positron annihilation study of defect distribution in 8YSZ nanostructure

Isabel Gonzalo-Juan [a], Paola Parente [b,*], Antonio Javier Sanchez-Herencia [c], Fausto Rubio [c], Ramiro Pareja [b], Begoña Ferrari [c]

[a] Department of Physics and Astronomy, Vanderbilt University, 2201 West End Ave., Nashville, TN 37235, United States
[b] Department of Physics, Universidad Carlos III de Madrid, Avda. Universidad 30, Leganés, 28911, Spain
[c] Instituto de Cerámica y Vidrio, CSIC, C/ Kelsen 5, Madrid, 28049, Spain

Abstract: The impact of the interfacial contribution on overall properties increases with decreasing grain size of polycrystalline materials. It is well known that distribution and size of cluster defects are rather different in bulk than grain boundaries. In light of "bottom-up" approaches, a study at the atomic level determining the distribution of crystallographic defects could clarify their contribution to the macroscopic properties, and then differentiate materials for outstanding or precise applications. In this work, Positron Annihilation Spectroscopy (PAS) is used to characterize the distribution of defects within 8 mol% Y_2O_3-stabilized zirconia (8YSZ) structures prepared by sintering through three different thermal treatments, i.e. a conventional thermal cycle in air and N_2/H_2 atmosphere, and a fast firing cycle in air, which lead to average grain sizes <260 nm.

1. Introduction

The description of size effects and associated conduction mechanisms is a main objective of research within nano-ionics [1,2]. Although the morphological characteristics of powders and materials prepared need further optimization, the discovery of electronic conductivity and large oxygen diffusivity at low temperatures, when the grain size is within the nanometric range in traditional ionic conductors [3,4], opened up a very exciting prospect of study inside the field [5].

In materials with fine grain size the density of grain boundaries is extremely high and transport along the grain boundaries might become dominant. Furthermore, in such materials the space charge regions adjacent to the grain boundaries might play a significant role. In fact, when grain size approaches width of space charge region (Debye screening length, λ), defects distribution significantly differs from the one characteristic of regular bulk materials. For small grains, local charge neutrality is not satisfied anywhere [4].

Otherwise, the concept of grain boundary regions supporting a fast ionic transport mechanism is still poorly understood [4–8]. The explanation for enhanced conduction at boundaries is also related to the formation of the space charge regions adjacent to the core in the grain boundaries. Bulk ionic defects with charge like to that of the boundary core will be depleted while those with opposite charge will be accumulated in the space charge region. If the bulk defect with high mobility is accumulated in the space charge region, the overall conductivity of the solid should increase. So, results reported in the literature suggest that grain boundaries can play a significant role in changing from ionic to electronic conductivity [9]. For example, oxygen vacancy distribution in a nano-structured zirconia based material determines phenomena such as ionic conductivity, electronic conductivity and, moisture-induced degradation [10,11] or protonic conduction, due to water incorporation in the zirconia lattice [12,13]. Efficient method and material strategies of directing or enhancing the space-charge effects, such as the introduction of interfaces or doped grain boundaries with surface active second-phase particles, have been successfully proposed [1].

However, description of macro-sized effects of the atomic architecture design is still challenging. It is evident that control of dimensions on the nanoscale has a profound influence on performance. Preparation of nanostructured materials has been made possible through the development of synthesis, processing and sintering routes, but direct characterization of prepared structures has still to be explored. Positron Annihilation Spectroscopy (PAS) was used to investigate the effects of sintering conditions on the microstructural features of the Y_2O_3-stabilized zirconia samples (YSZ). PAS is a non-destructive successful technique used to study the occurrence, nature and evolution of defects in solids [14,15], particularly lattice point defects, which cannot be detected by other techniques. PAS takes advantage of the fact that positrons are attracted to atomic-size open-volumes, where positively charged atomic nuclei are missing [16], that act as trapping centers for positrons that subsequently annihilate with electrons in that area. As a result of trapping, measurable changes in the positron annihilation

* Corresponding author at: Present address: Instituto de Cerámica y Vidrio, CSIC, C/ Kelsen 5, Madrid, 28049, Spain. Fax: + 34 91 7355843.
E-mail address: pparente@icv.csic.es (P. Parente).

characteristics are seen that make the identification of vacancy-type defects straightforward [17]. When an energetic positron from a radioactive isotope source enters a solid, it loses most of its energy by collisions with electrons and ions within a few ps, to reach a level of energy of the order of k_BT (k_B is the Boltzmann factor and T is the temperature of the solid). Then it diffuses into the material for a length L_+ of the order of 100 nm [16] ($\approx$150 nm according to Ref. [18]) until annihilates by interaction with an electron, after its specific lifetime in the crystal, giving off information about the annihilation site. The whole diffusion distance is of the order of magnitude of 100 μm and the information is in the form of gamma rays, giving the positron–electron annihilation primarily two 511 keV gamma rays travelling in opposite directions (in the center of mass frame) [19]. Positron lifetime (PL) and coincidence Doppler broadening (CDB) modes of PAS were used in the present work. PL reflects the local electron density at the annihilation site and gives information about the size of the positron traps and their concentration. The CDB measurements of the annihilation radiation provide data about the momentum distribution of electrons taking part in the positron–electron annihilation. The energies of the two emitted 511 keV photons present a blueshift and a redshift (Doppler broadening) in the laboratory frame related to the momentum of the electron–positron pair prior to positron annihilation. The energy shift of each of the two photons is given by:

$$\Delta E = p_L c / 2 \tag{1}$$

where p_L is the longitudinal momentum shift and c is the speed of light. The shifts of the two photons are measured simultaneously in CDB. Since the thermalized positron has an almost zero momentum, and each element has its own characteristic orbital electron momentum spectrum [19], then a measure of Doppler effect of the annihilation radiation supplies information on the electronic structure of materials and the chemical surroundings of the annihilation sites [18].

The PAS technique has been used previously for characterizing ceramics [20–23] including zirconia [18,19,24,25]. It turned out to be an important tool of investigation of nanostructed YSZ materials [18], being the study of the interaction of positrons with point defects and grain boundaries in zirconia useful to get a deeper insight into the microstructure of such complicated systems.

When the trivalent oxide Y_2O_3, is added to ZrO_2 as stabilizer, lattice defects like oxygen vacancies and negatively charged substitutional solutes are created in the ZrO_2 lattice. The defect reaction can be written, using the Kröger–Vink notation for point defects [26], as:

$$Y_2O_3 \xrightarrow{ZrO_2} 2Y'_{Zr} + 3O_O^X + V_O^{\cdot\cdot} \tag{2}$$

$V_O^{\cdot\cdot}$ and Y'_{Zr} having, respectively, +2 and −1 charge respect to the lattice, represent the main defects in bulk zirconia. However, because of coulombic interaction between charged defects, a large amount of negative oxygen vacancies and vacancy-solute atom complexes result in the lattice. At low temperatures only a relatively small fraction of free oxygen vacancies are present as unassociated [19]. The majority tends to be present as associated with substitutional yttrium, forming $Y'_{Zr}V_O^{\cdot\cdot}$ [27,28] complexes at low yttrium concentration and more complex associates, such as $Y'_{Zr}V_O^{\cdot\cdot}Y'_{Zr}$, with a higher yttrium concentration [19]. Due to their strong positive charge, $V_O^{\cdot\cdot}$ are not likely to attract positrons, but the associated defects $Y'_{Zr}V_O^{\cdot\cdot}$ and $Y'_{Zr}V_O^{\cdot\cdot}Y'_{Zr}$ have a low or no positive charge and so can interact with positrons. Other possible defects with a negative charge, such as V_{Zr}'''' occur in low concentrations [19].

In nanocrystalline materials grain boundaries and defects associated with them have a significant role in Positron Annihilation Spectroscopy. In fact, being the positron diffusion length L_+ comparable to the mean grain size, positrons thermalized inside the grains can easily reach grain boundaries during their lifetime by their diffusion motion, thus probing those regions and becoming trapped there. It is known that grain boundaries in compacted nanocrystalline powders have a highly defective structure with a high density of open-volume defects [29]. Hence, one can expect that positrons become trapped and annihilate in these open-volume sites [18]. In ionic materials the grain boundary core is characterized by a fairly strong positive charge with a concomitant negatively charged space-charge region that compensates the positive potential. In YSZ the latter region is proved to be characterized by low oxygen vacancy concentration and a correspondingly high yttrium-ion concentration [19], thus being a likely trapping region for positrons. The positive grain boundary core repels positron, but the size of the potential barrier (a few tenths of eV) does not prevent positrons from getting trapped in much deeper positron potential wells at the space charge zone of the grain boundaries [10,18,30].

2. Experimental

2.1. Preparation and crystallographic/morphologic characterization of YSZ powders and compacts

The following commercially available cubic ZrO_2 stabilized with 8 mol% Y_2O_3 nanocrystalline powders (8YSZ, Nanostructured & Amorphous Materials, Inc., USA) was used as starting material, with a mean particle size of 60 nm and the following chemical analysis (wt.%): Y_2O_3 (13.3), HfO_2 (2–3), Al_2O_3 (0.01), Fe_2O_3 (0.01), SiO_2 (0.02) and Na_2O (0.01).

The specific surface area of the powders and density were measured by one point N_2 adsorption (monosorb, Quantachrome, USA) and He-multipicnometer (Quantachrome, USA), respectively. The errors of those techniques are ±5% and ±10%, respectively. The particle size distribution and the zeta potential of nanoparticles were determined by dynamic light scattering and laser Doppler velocimetry, respectively (Zetasizer Nano ZS, Malvern S, UK). In order to carry out particle size distribution and zeta potential measurements, basic aqueous suspensions ($pH = 9$) of 8YSZ powders with solid contents of 10^{-3} g l^{-1} were prepared.

The green compacts were obtained by cold isostatic pressing (CIP) of powders at 200 MPa. In order to select the optimum temperature range to obtain sintered 8YSZ samples with high porosity, dynamic sintering experiments were performed on prismatic samples (6 mm × 4 mm × 4 mm) using a push-rod dilatometer (Netzsch, Germany) in air or under flowing atmosphere of N_2/10 vol.% H_2. Tests were recorded at temperatures up to 1450 °C at heating and cooling rates of 5 °C min^{-1}. Two hours dwell thermal treatment at 1250 °C, using 5 °C min^{-1} as heating and cooling rates, was performed in N_2/H_2 (8YSZ-N_2/H_2) and air (8YSZ-Air) atmospheres. A fast firing cycle (FF) [31] in air was also considered (8YSZ-FF). The FF cycle was composed of a fast heating ramp of 20 °C min^{-1} up to a temperature of 1250 °C followed by a 20 hour dwell at 1150 °C after a cooling ramp of 15 °C min^{-1}. FF was performed in a tubular furnace with flowing atmosphere (Severn Furnaces Limited, UK) which uses a Eurotherm programmer. When it was necessary the sintering atmosphere was purged prior to heating by applying vacuum to the sealed tube and filling it with the desired gas. During the thermal cycle the gas flow was maintained. All the gases were of high purity standards.

Phase identification of the as-received powders and sintered samples was carried out by XRD with a diffractometer (D5000, Siemens, Germany) using a Cu Kα radiation collected at room temperature over a range of $20° \leq 2\theta \leq 80°$ at a step scan rate of 2°s^{-1}. The results were processed using the ASTM-Files 37–1484, 48–0224 and 82–1246 for monoclinic, tetragonal and cubic phases, respectively. Furthermore, phase identification was also performed by Raman Spectroscopy using the 514.5 nm excitation line from an Ar ion laser (Spectra Physics 163-M42-010) in backscattering geometry on a

RENISHAW in Via spectrometer. Laser power of 25 mW was used, and spectra were collected over an effective range of 100–700 cm^{-1}.

The apparent density of sintered samples was determined by the Archimedes method in water. The relative density was calculated using the theoretical density of the YSZ (5.90 g cm^{-3}, ASTM 82-1246). Densities of the solid skeletons were determined by helium pycnometry. Porosity of the samples was measured using a Hg-porosimeter (Poromaster, PM-338, Quantachrome Instruments, USA).

The microstructure of the sintered samples was observed by field emission scanning electron microscopy (FE-SEM, Hitachi, S-4700, Japan) on polished and thermally etched surfaces. Thermal etching at 1150 °C for 1 h was used. Average grain sizes of the microstructures were determined on FE-SEM micrographs by the linear intercept approach (average grain size = 1.56 average intercept length) [32].

2.2. PAS apparatus and data acquisition process

PL and CDB techniques of positron spectroscopy were applied in order to characterize the microstructure of zirconia samples. All the experiments were performed at room temperature using a Na^{22} positron source of ~10 μCi sealed between two kapton foils (10 μm thick). For each measurement, the positron source was sandwiched between two identical samples. Positrons emitted from Na^{22} sources have energies up to 0.54 MeV, giving a typical implantation depth of the positrons into YSZ materials of ≈130 μm.

The PL setup was a commercial fast-fast ORTEC system equipped with two NE111 plastic scintillator detectors placed face to face and each in contact with the pair of samples enclosing the positron source. The detectors reveal γ radiation corresponding both to the positron emission and to the annihilation signals. The pulses from the detector were used as the start and stop of a time to amplitude converter (TAC), which measures the time interval between the two signals and generates a pulse of intensity proportional to the interval and then to the positron lifetime. The corresponding digital pulses were analyzed by a multichannel analyzer (MCA), which displayed them in a graph representing the channels corresponding to fixed time intervals on the x axis, and the number of annihilation events corresponding to the channels on the y axis. This is the lifetime spectrum which is characterized by an exponential decaying part given by the convolution of several components, each of which related to a positron annihilation state and then to a characteristic positron lifetime. The lifetime spectra were analyzed and decomposed into individual discrete components using the POSITRONFIT [33] program, after subtraction of the source component and deconvolution of the experimental resolution function approximated as a Gaussian. Reduced χ^2 of data analysis was never higher than 1.2. Each cumulative spectrum had at least 10^6 counts. In the condition of the present experiment, the time resolution of the system (full width at half maximum of the resolution function) was 278 ps.

CDB experiments were performed using an apparatus with two HP Ge detectors in timing coincidence, placed face to face and separated 40 cm from each other. The pair of samples, enclosing the positron source, was positioned just at the half-way point between the detectors. Each detector was connected to an ORTEC-572 amplifier which gain was adjusted to have exactly the same calibration factor for both detectors (81.1 eV channel^{-1}). Signals from the amplifiers were fed into a two-dimensional multichannel analyzer (2D-MCA) adjusted to focus the peak of 511 keV at the center of a 512×512 matrix. The cumulative CDB spectra had ~10^7 counts in the strip centered on the matrix diagonal that fulfilled the condition $2m_0c-1.6$ keV$<E_1+E_2<2m_0c^2+1.6$ keV; where E_1 and E_2 denote the energy of the annihilating gamma-ray pairs, m_0 is the electron rest mass, and c is the light speed. To accentuate the difference between the CDB spectra, and to visualize the defect effect on the intensity of the peaks, the spectra were normalized, dividing the counts at a given energy by that corresponding to a high purity Zr sample and to the YSZ single crystal. Previously, the areas under the CDB spectra were normalized to unity and smoothed.

Well-annealed high-purity Zr and cubic YSZ single crystal were used in the preset work as reference specimens for the CDB spectra analysis. The samples were also examined by PL measurements for completeness and clarity.

3. Results and discussion

The specific surface area and density of the as-received powder are 17.8 m^{2}g^{-1} and 5.69 g cm^{-3}, respectively. Scanning Electron Microscopy (SEM) morphology of as received powders showed 100 μm agglomerates of atomized powder formed by spherical shaped 8YSZ nano-particles of around 50 nm primary particle size [34]. Assuming monodispersed and spherical particles, an average diameter was calculated using the adsorption model from the nitrogen adsorption isotherm (d_{BET}) leading to particles with an average size of 60 nm. The BET approximation fit SEM observations. Particle size distribution after sonication treatment [34] shows a monomodal size distribution curve with a narrow particle population in the nanometric range (<100 nm), being 84 nm the average particle size. Therefore, supplied nanopowders were weakly agglomerated because it was possible to disperse particles down to an average size close to the primary particle size by applying a low energy to break them.

Dynamic sintering studies performed on compacts of 8YSZ, obtained by isostatic pressing, under both air and N$_2$/H$_2$ atmosphere for compacts are plotted on Fig. 1. The curve for a YSZ sub-micrometric particle compact in air is also plotted for comparative purposes [35]. For nanometric powders it can be observed that sintering starts at 1050 °C under both air and reductive atmosphere. The maximum shrinkage rate of these samples takes place around 1250 °C, being achieved slightly earlier in air. Densification finishes around 1500 °C and 1450 °C with a final shrinkage of 20% in air and 23% for the N$_2$/H$_2$ treatment. In the case of sub-micrometric particle compacts, the sintering process starts at a lower temperature than nanometric ones, but it progress slower with and finishes at lower temperatures. Temperatures were extracted from the derivative curves which can be reached as supplementary data in the electronic version. The final shrinkage recorded in air for compact made of submicrometric powders is similar to that of the sample made of nanostructured powders and treated under N$_2$/H$_2$. Finally a thermal treatment at 1250 °C during 2 h was selected to sinter bulk pieces of nano-powders in air (8YSZ-Air) and reductive (8YSZ-N$_2$/H$_2$) conditions. Complementarily, a fast firing thermal cycle was designed with a top temperature of 1250 °C selected to compare results done through conventional cycles, while the dwell temperature has been
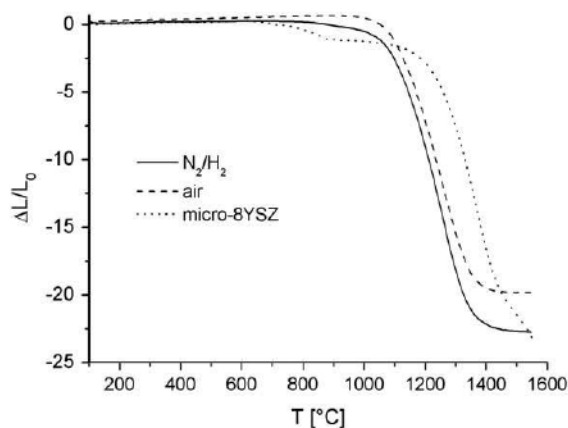

Fig. 1. Dynamic sintering curves recorded for 8YSZ compacts of nanopowders in air and under reductive conditions, and submicrometric particles in air. $\Delta L/L_0$: linear shrinkage, *vs.* temperature.

selected following previous works in the literature [6,31,36] and the temperature of neck formation in air of 8YSZ nanoparticles fitted at the dynamic sintering study (1050 °C in Fig. 1).

Apparent density and porosity of the sintered compacts (8YSZ-Air, 8YSZ-N$_2$/H$_2$ and 8YSZ-FF) are collected in Table 1, while Fig. 2 shows porous diameter distributions measured by Hg porosimetry. The values of the apparent density measured by Archimedes method in H$_2$O were always within the variability limits of those calculated from Hg porosimetry results. Results in Table 1 and Fig. 2 show that thermal treatments led to specimens with a high level of open porosity, ranging 24%–39%, while closed porosity can be neglected (<0.1%). Porosity decreases in 8YSZ-N$_2$/H$_2$ and 8YSZ-FF compacts, both specimens being denser than that sintered in air through a conventional thermal cycle (8YSZ-Air). Between non-conventional cycles, porosity is higher in 8YSZ-FF both in volume and size than in 8YSZ-N$_2$/H$_2$. Apparent density determined by Archimedes method led to higher values of density for 8YSZ-FF, verifying the presence of large pores that can be filled by water, in agreement with plot in Fig. 2. Then, porosimetry proved to be an accurate technique to determine density in nanostructured 8YSZ compacts, determining pore coalescence in the case of the fast firing treatment. Compact densities fit sintering studies, suggesting that reductive and fast firing thermal treatments promote the 8YSZ structure densification. The size of pores in all samples is within the nanometric range, although the high level of porosity.

SEM micrographs in Fig. 3(a) and (b) show a fresh fracture of the 8YSZ-Air specimen, at low and high magnification respectively. Fracture image at low magnification remembers the characteristic morphology of atomized powders, while a detail of this image (Fig. 3(b)) reveals the transgranular fracture of a dense structure of zirconia composed by grains around 250 nm in size. Fracture behavior releases the apparent density dependence of the sintered compacts on as-received powder morphology, which can be the cause of the high volume of open porosity of isostatic pressed samples whatever was the thermal treatment. A meticulous look at the microstructure at higher magnifications also highlights small interconnected voids which also contribute to the low apparent density of 8YSZ-Air compacts measured in water (Table 1).

Fig. 4 shows FE-SEM micrographs of the thermally etched polished surfaces of 8YSZ samples sintered in air (8YSZ-Air, Fig. 4 (a) and (b)) and in N$_2$/H$_2$ atmosphere (8YSZ-N$_2$/H$_2$, Fig. 4 (c) and (d)) with a conventional cycle and in air through the fast firing treatment (8YSZ-FF, Fig. 4 (e) and (f)). The average grain size of these sintered compacts is 256, 128 and 167 nm, respectively. It can be observed that the 8YSZ-N$_2$/H$_2$ compact shows an average grain size smaller than the 8YSZ-Air sample. In fact, the conventional sintering cycle in air leads to a porous network within 8YSZ nanostructure which is not present at the 8YSZ-N$_2$/H$_2$ and 8YSZ-FF microstructures, verifying a higher densification level under the reductive and fast firing thermal cycles.

Microstructures agree with shrinkage dynamic tests and density studies. 8YSZ compacts has a faster but lower contraction in air than in N$_2$/H$_2$, resulting in a higher volume of porosity in air, but a similar
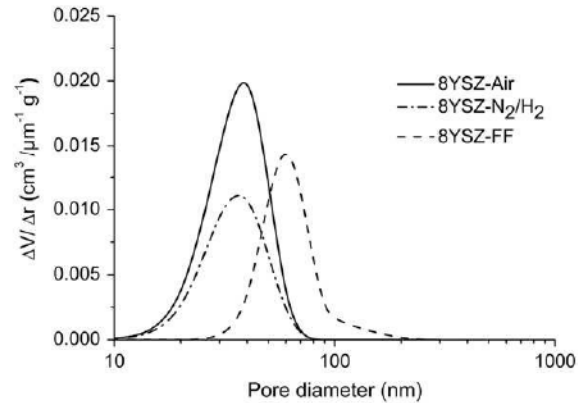

Fig. 2. Pores distribution in 8YSZ compacts.

pore size at the microstructure. Otherwise, the fast firing process promotes densification decreasing the porosity volume and increasing the pore size due to a size coalescence effect through the lower dwell temperature (1150 °C) [6,36].

Fig. 5 shows the X-Ray Diffraction (XRD) spectra recorded for the 8YSZ-Air and 8YSZ-N$_2$/H$_2$ samples. The spectrum of the as-received powder was also plotted for comparative purposes. The latter spectrum reveals the presence of monoclinic, tetragonal and cubic phases at the as-received nano-particles, while the XRD pattern of the sample sintered in air reveals the presence of the monoclinic and cubic phases in the 8YSZ-Air compact. Finally, the XRD spectrum corresponding to the 8YSZ-N$_2$/H$_2$ compact shows the presence of both tetragonal and cubic phases and a remarkable absence of the monoclinic phase.

Table 1
Density and porosity values of the 8YSZ compacts sintered at 1250 °C for 2 h (8YSZ-Air) and at fast firing conditions in air (8YSZ-FF) and at 1250 °C for 2 h under N$_2$/H$_2$ atmosphere (8YSZ-N$_2$/H$_2$). ρ_{H_2O}: determined by immersion in water; ρ_{He}: determined by helium pycnometry.

Thermal treatment		8YSZ-Air	8YSZ-FF	8YSZ-N$_2$/H$_2$
Apparent density[a]: ρ_{He}	[g·cm^{-3}]	5.85 ± 0.05	5.86 ± 0.05	5.86 ± 0.05
	[%]	>99	>99	>99
Apparent density[b]: ρ_{H_2O}	[g·cm^{-3}]	4.1 ± 0.3	5.4 ± 0.3	4.8 ± 0.4
	[%]	70 ± 2	91 ± 2	82 ± 2
Total porosity[c]	[%]	39.3 ± 0.1	32.2 ± 0.1	23.8 ± 0.1
Average porous size[c]	[nm]	45	65	40

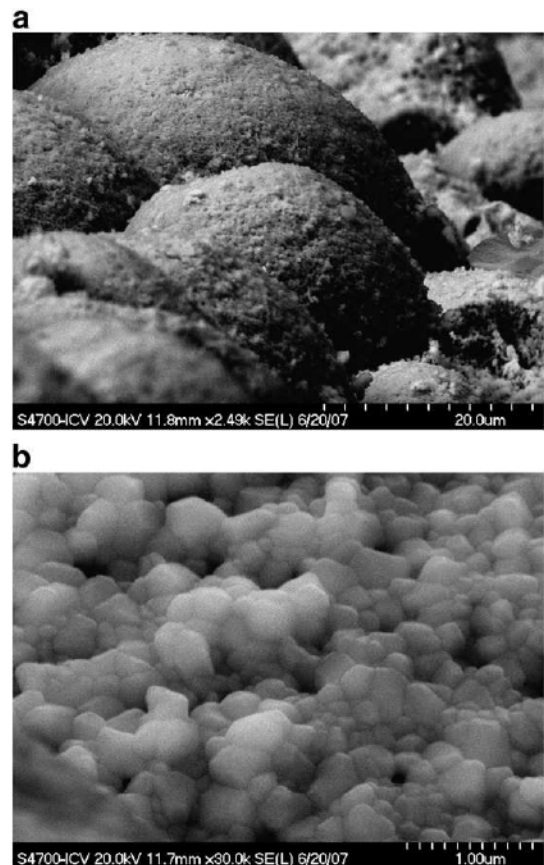[a]He picnometry; [b]Archimedes method in H$_2$O; [c]Hg porosimetry.

Fig. 3. General view (a) and a detail (b) of the fracture surface of 8YSZ-Air.
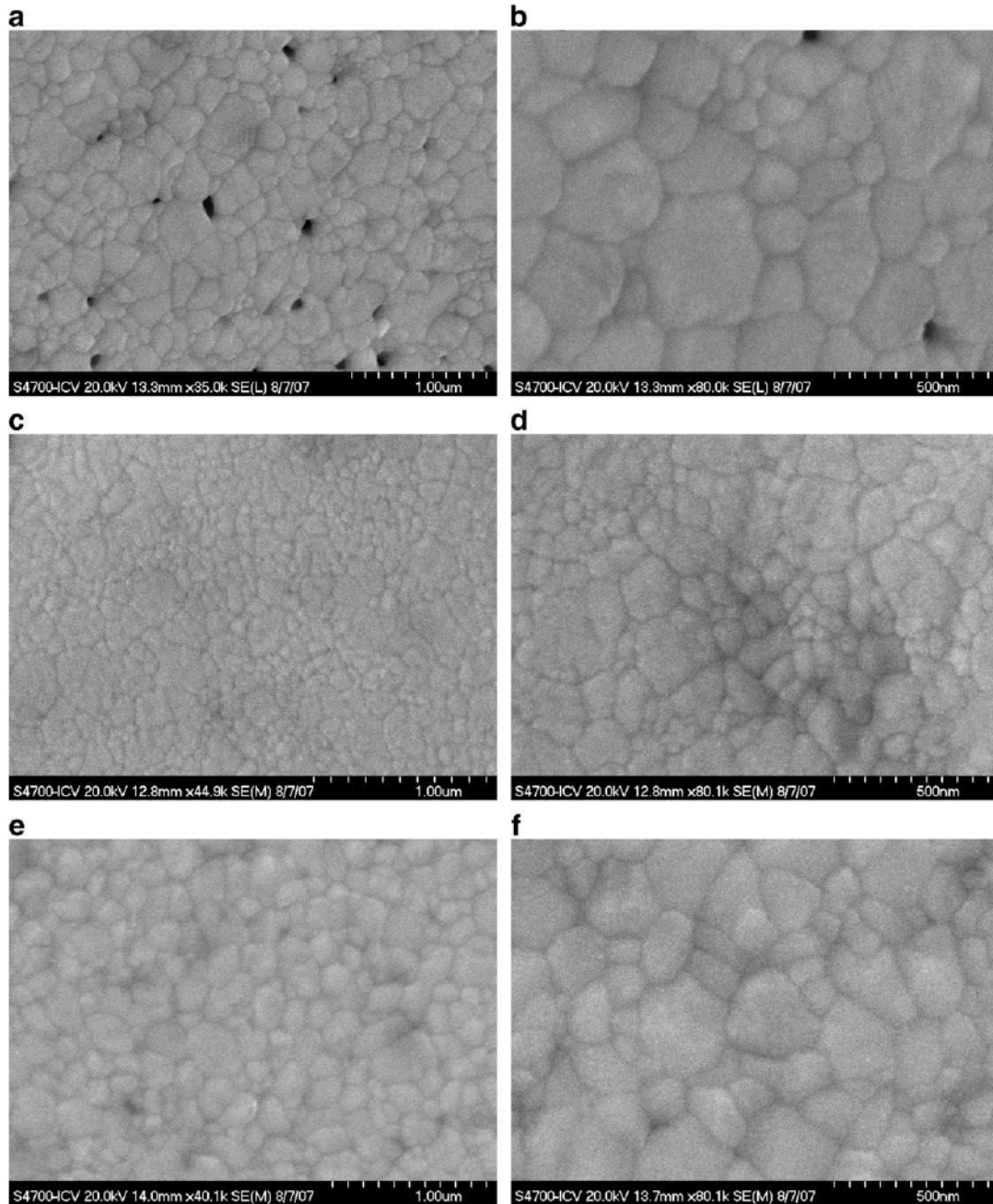
Fig. 4. Polished surfaces of the 8YSZ samples sintered at 1250 °C for 2 h in air (a, b) and in N_2/H_2 atmosphere (c, d), and through a fast firing cycle (e, f) in air, being thermally etched at 1150 °C/1 h in air and under reducing conditions, respectively.
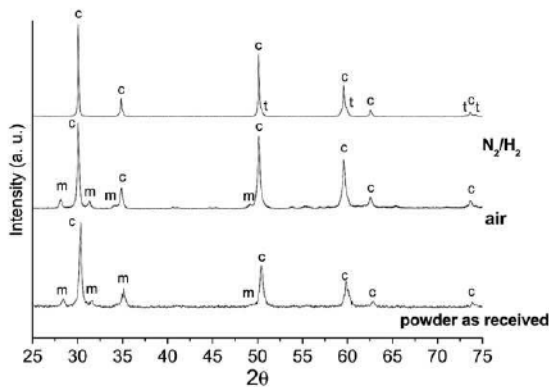

Fig. 5. XRD patterns of 8YSZ as received powders and compacts sintered at 1250 °C for 2 h in air and under N_2/H_2 atmosphere.

In the case of 8YSZ powders FT-Raman spectroscopy is a technique more sensitive than XRD not only for establishing the major phase but also to assess the presence of minor phases. The Raman spectra of the 8YSZ-Air and 8YSZ-N_2/H_2 are depicted in Fig. 6. The characteristic band of cubic zirconia phase at 607 cm^{-1} can be observed in both samples. In addition, both samples show the characteristic bands corresponding to tetragonal phase zirconia, but characteristic bands of monoclinic zirconia phase are only identified in powders treated in air, determining definitely the absence of the monoclinic phase at the 8YSZ compacts sintered under reductive atmosphere. Hence we can consider that during the sintering treatment under N_2/H_2 atmosphere the monoclinic-tetragonal phase transition took place.

In addition to vacancies produced by substitution of zirconium cations for yttrium trivalent cations, new defects can be introduced by sintering in reducing atmosphere [37–39]. In fact, the concentration of
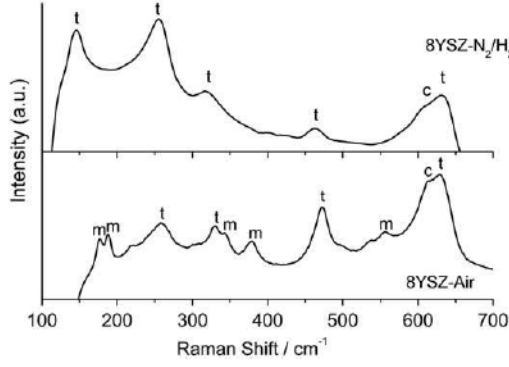
Fig. 6. Raman spectra of 8YSZ compacts sintered at 1250 °C for 2 h in air and under N_2/H_2 atmosphere.

oxygen vacancies and electrons are linked to oxygen partial pressure during thermal treatment [37,40]. Stabilization studies of the zirconia phases by the presence of oxygen vacancies [41] could explain the absence of monoclinic phase as well as the full stabilization of tetragonal and cubic phases shown by Raman spectroscopy for 8YSZ-N_2/H_2 specimens.

Otherwise, sample darkening in reducing atmosphere was associated to the presence of oxygen vacancies [42–44] and/or the segregations of iron impurities at the grain boundaries [40]. Segregation of second phases is commonly associated to an increase of bond-length at the crystal structures in the grain-boundary neighborhood leading to a high grain boundary separation [45]. Therefore, nanostructure of 8YSZ-N_2/H_2 compacts, observed in Fig. 4(c) and (d), could be the consequence of the increase of vacancies and/or second phase segregation in the grain boundary. 8YSZ-darkening and the absence of monoclinic phase being the remarkable evidence of this phenomenon.

Positron lifetime spectra of 8YSZ compacts were studied. Annihilation curves were resolved into 3 components each characterized by a positron lifetime (τ_1, τ_2, τ_3) with a certain intensity (I_1, I_2, I_3; $\sum_i I_i = 1$) and the results are summarized in Table 2. Results of measurements on well-annealed high purity Zr and 8YSZ single crystals were also reported, showing that these specimens exhibit a single lifetime component. In all cases the long lifetime component ($1 < \tau < 3$ ns with intensity $\leq 1.5\%$) was assigned to annihilation of positrons in ortho-positronium state in free volume in the structure but it was not assigned to a particular type of voids because of its weak intensity. Neglecting this long component, we only considered and discussed the short lifetime components τ_1 and τ_2. Applying the simple two-state trapping model the bulk positron lifetimes $\tau_B = \left(\sum_i I_i/\tau_i \right)^{-1}$ were deduced and reported. Besides, the average positron lifetime defined by $\tau_{av} = \sum_i I_i \tau_i$ was evaluated since it is a statistically accurate single parameter to describe a lifetime spectrum [17], and changes below 1 ps are reliably observed [17]. A value of $\tau_{av} > \tau_B$ (free-positron lifetime in the bulk) is the direct manifestation of positron trapping in vacancy-type defects [17]. In the present case it is an evidence of the presence of structural vacancies in the three 8YSZ sintered samples.

The single lifetime component of ≈ 184 ps measured for the single crystal was attributed to annihilation inside the grain and related to structural defects. In analogy with the single crystal, one expect that nanocrystalline ceramics contain a relatively high density of structural defects [18] and that they contribute to PL spectrum by a component with lifetime of ≈ 184 ps. This component and one with a higher value due to trapping of positrons to defects related to grain boundaries, could hardly be distinguished if their lifetimes are closely spaced (the separation of two different lifetimes is successful only if the ratio of their values is >1.5 [17]). In this case contributions from the annihilation inside the grains and that at grain boundaries were revealed as a single component: the lifetime τ_1 measured for 8YSZ samples, >184 ps (see Table 2).

The high value of the intensity of this component (I_1) indicates that the inside of the grains and their space charge regions have a high defect density, so that positrons mainly become trapped and annihilate there. Indeed, as mentioned above, vacancy-type defects in the negatively charged region of grain boundaries of such nanocrystalline materials are likely trapping centers for positrons.

It can be noted that the sample 8YSZ-N_2/H_2 presents a value of τ_1 slightly lower than that of 8YSZ-Air and 8YSZ-FF. It can be considered an unexpected result, since a smaller grain size should lead to a greater contribution of the annihilation at the space charge region, and then, to a higher lifetime value due to a higher fraction of positron reaching the grain boundary and the increase of the interface-to-bulk fraction [4]. Actually, the decrease in τ_1 value in 8YSZ-N_2/H_2 specimens can be firstly attributed to the absence of monoclinic phase after reducing treatment (Fig. 6). As this is related to a variation of the electron state, it determines a higher electron density in c- and t-phases than in m-phase [4,25,46]. Moreover, the effects of N_2/H_2 atmosphere over the distribution and the increase of defects should be also considered. Instead the anionic vacancies formation, unfavorable at such low temperature as 1250 °C, the electron concentration can increase in orders of magnitude under reducing conditions [37], resulting, in our case, in a higher probability of positron annihilation inside the smaller grains. Consequently, we could hypothesize a greater presence of defects along the structure, where positrons could be trapped enhancing their annihilation inside the grains rather than at the space charge region. According to the study of Maier [4] on concentration of defects in nanostructured materials, the impact of interfaces and particularly of their spacing on conductivity, we can speculate that the found lifetime values are related to the dependence of charge concentration on grain size. In ref. [4] it was stated the occurrence of "trivial" size effects, in which the increased overall effect solely relies on increased proportion of interfaces, and of "true" size effects, in which also the local properties are changed, that occurs when the grain size, L, is comparable with the Debye length λ ($L \leq 4\lambda$). We can suppose that the decrease of grain size due to the reductive thermal treatment is likely to determine the space charge overlap so that no electroneutral bulk is left, thus increasing annihilation of positrons in the interior of the grain and shortening their lifetime. The different mechanisms of annihilation in 8YSZ-N_2/H_2 samples are reflected also in a lower value of the average lifetime (see table of results), although within the limits of the error.

Table 2
Lifetime values measured for tested compacts. τ_{av} and τ_B were calculated applying the simple two-state trapping model and errors were calculated taking into account only the errors on lifetime values.

Material	τ_1 [ps]	I_1 [%]	τ_2 [ps]	I_2 [%]	τ_3 [ns]	I_3 [%]	τ_{av} [ps]	τ_B [ps][a]
Zr	164.4 ± 0.4	99.55 ± 0.05			1.3 ± 0.2	0.45 ± 0.05		
Single crystal	184.4 ± 0.6	99.52 ± 0.06			1.4 ± 0.2	0.48 ± 0.06		
8YSZ-Air	191 ± 3	95 ± 2	500 ± 100	4 ± 2	1 ± 2	0.2 ± 0.6	203 ± 7	196 ± 4
8YSZ-FF	192 ± 2	97.3 ± 0.4	800 ± 300	1.8 ± 0.4	3 ± 2	0.9 ± 0.5	203 ± 7	195 ± 2
8YSZ-N_2/H_2	188 ± 2	95.3 ± 0.8	600 ± 100	3.2 ± 0.6	2.3 ± 0.6	1.5 ± 0.3	201 ± 5	192 ± 2

[a] Deduced applying the simple two-state trapping model.

The second component (τ_2, being its intensity I_2), can be attributed to positron annihilation in vacancy clusters or nano-voids that can be effective trapping centers for positrons [19], as expected in such porous ceramics (>20%). Only a low portion of positrons cross the grain boundary and are trapped by pores (very low I_2), despite the high porosity of the nanostructure. It has to be recalled that the lifetimes measured for positrons trapped in a certain defect type are sensitive to the defect size, while the respective intensities provide information about the defect concentration [18]. Lifetime values and intensity of this second component fit with the apparent density measured by Archimedes method in H_2O and Hg porosimetry (see Table 1), reflecting changes in size and distribution of pores as a result of the thermal treatments. In fact, as previously observed, these promote the densification and the disappearance of nanopores, particularly accompanied by pore clustering in the fast firing process. This later treatment produces a coalescence of open-volume defects resulting in a wider size distribution of pores (corresponding to maximum τ_2 value and related error) and a reduced concentration (minimum I_2).

CDB spectra are shown in Figs. 7 and 8. The spectra were normalized and to well anneal zirconium (Fig. 7) and to a single crystal of fully stabilized zirconia (Fig. 8). The spectrum of the single crystal and Zr were acquired as a reference and reported for comparison.

In general two parts of a CDB spectrum can be distinguished: the low-momentum ($\leq 6 \times 10^{-3} m_0 c$) region that is related to annihilation with valence electrons and reveals the relative concentration of defects, and the one of higher-momentum due to core electrons [18]. In the present spectra, the signal in the low-momentum region is related to positron annihilation in nanopores, while the peak centered at $\approx 20 \times 10^{-3} m_0 c$ in the high-momentum region is characteristic of annihilations with valence electrons of oxygen ions in the lattice [19]. In this region the difference between the ratio curves for pure Zr and ZrO_2 samples observed in Fig. 8 suggests that the predominant annihilation sites in the bulk areas (core electrons) of the sintered samples are near oxygen, not zirconium [19]. It is confirmed by the results of normalization of the curves to pure Zr, which show the characteristic peak of annihilations with oxygen in the lattice [19].

In Fig. 8 it can be observed that the CDB spectra of the three 8YSZ samples and the single crystal fit a same general trend. The CDB spectrum of the sample sintered in air (8YSZ-Air) has higher low-momentum intensity than that of samples sintered in reducing atmosphere (8YSZ-N_2/H_2) and through the fast firing cycle (8YSZ-FF). The intensities in the low momentum-region and their changes are the consequence of densification and the disappearance of nanovoids related to the thermal treatments. The fact that the curves approach that obtained for the single crystal is due to the low fraction of
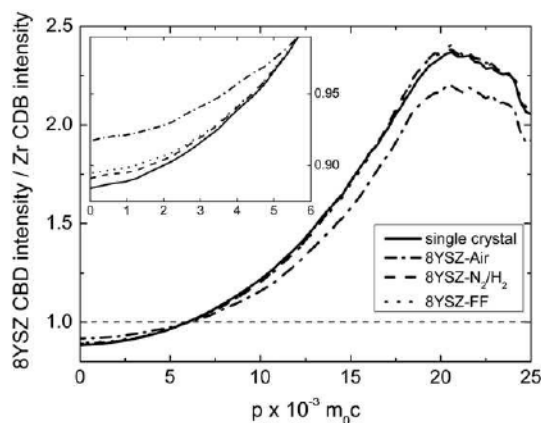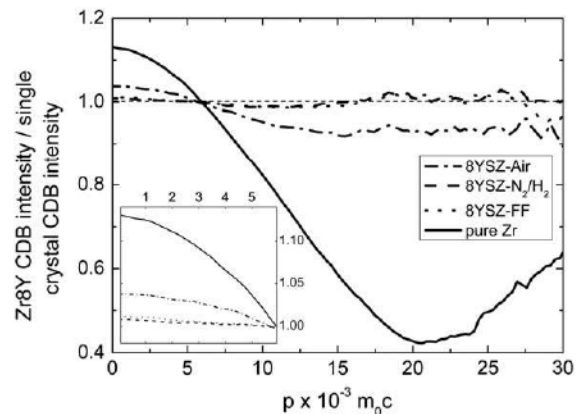

Fig. 8. CDB ratio curves to single crystal for YSZ and pure Zr. The detail points out variation in intensity in the low-momentum region.

positrons annihilating at pores. CDB spectra verify the high defect density in the whole structure as observed before.

Summarizing, PAS studies revealed an extremely high intensity of the first lifetime component, I_1, as a consequence of an elevated defect concentration within the nanostructure of all the samples. CDB normalized spectra of 8YSZ-FF and 8YSZ-N_2/H_2 compacts are similar to those of the single crystal, even considering the increase of density of grain boundaries in the nanostructure. In fact, the first lifetime component, τ_1, in the smallest nanostructure tested (8YSZ-N_2/H_2) is closer to that of the single crystal, due to the increase of the electron density promoted by the conditions of the sintering treatment. PAS results agree with studies supporting electronic conduction and the absence of the structure electroneutrality at the nanoscale in such a kind of ionic materials.

4. Conclusions

PAS results (of PL and CDB analysis) were related to the morphological and crystallographic characteristics of 8YSZ materials, and well known theories of solid state ionic materials, such as space charge region distribution in nanostructures. The characterization of prepared 8YSZ materials led to differences on defect distribution in nano-ranged structures with an average grain size <260 nm.

Defect distribution along the sintered structure changed depending on the thermal treatment. Fast firing cycle and reducing atmosphere gave crystallographic variations and a defect re-distribution at grain boundaries. Long sintering cycle produced average grain sizes of 167 nm and an effect of pore coarsening. However, sintering under reducing atmosphere promoted densification and grain size retention down to 126 nm, and simultaneously an increase of the electronic density along the structure. In 8YSZ-N_2/H_2, concentration of defects increased, the defects being confined in a small grain. The final result was the augment of defectivity in the whole structure (bulk and grain boundaries).

Finally, PAS was validated as a powerful technique to describe the structure ordering at the atomic level, and then it can complement the characterization of conductive solids at the nanoscale.

Supplementary materials related to this article can be found online at doi:10.1016/j.ssi.2011.03.007.

Fig. 7. CDB ratio curves to pure Zr for YSZ and single crystal. The detail points out variation in intensity in the low-momentum region.

References

[1] J. Maier, Nat. Mater. 4 (2005) 805–815.
[2] L. Malavasi, C.A.J. Fisher, M.S. Islam, Chem. Soc. Rev. 39 (2010) 4370–4387.
[3] U. Brossmann, G. Knöner, H.-E. Schaefer, R. Wurschum, Rev. Adv. Mater. Sci. 6 (2004) 7–11.
[4] J. Maier, Solid State Ionics 157 (2003) 327–334.
[5] H.L. Tuller, Solid State Ionics 131 (2000) 143–157.
[6] M. Han, X. Tang, H. Yin, S. Peng, J. Power Sources 165 (2007) 757–763.
[7] I. Kosacki, T. Suzuki, V. Petrovsky, H.U. Anderson, Solid State Ionics 136–137 (2000) 1225–1233.
[8] I. Kosacki, C.M. Rouleau, P.F. Becher, J. Bentley, D.H. Lowndes, Solid State Ionics 176 (2005) 1319–1326.
[9] P. Knauth, Solid State Ionics 177 (2006) 2495–2502.
[10] X. Guo, R. Waser, Prog. Mater. Sci. 51 (2006) 151–210.
[11] X. Guo, J. He, Acta Mater. 51 (2003) 5123–5130.
[12] G. Chiodelli, F. Maglia, U. Anselmi-Tamburini, Z.A. Munir, Solid State Ionics 180 (2009) 297–301.
[13] U. Anselmi-Tamburini, F. Maglia, G. Chiodelli, P. Riello, S. Bucella, Z.A. Munir, Appl. Phys. Lett. 89 (2006) 163116, 163113 pp.
[14] R. Krause-Rehberg, H.S. Leipner, Positron Annihilation in Semiconductors: Defect Studies, Springer, Berlin, 1999.
[15] T.E.M. Staab, R. Krause-Rehberg, B. Kieback, J. Mater. Sci. 34 (1999) 3833–3851.
[16] M.J. Puska, R.M. Nieminen, Rev. Mod. Phys. 66 (1994) 841–897.
[17] P. Hautojarvi, C. Corbel, Proceedings of the International School of Physics 'Enrico Fermi'. Course CXXV. Positron Spectroscopy of Solids, 1995, pp. 491–532.
[18] J. Cizek, O. Melikhova, I. Prochazka, J. Kuriplach, R. Kuzel, G. Brauer, W. Anwand, T.E. Konstantinova, I.A. Danilenko, Phys. Rev. B 81 (2010) 024116.
[19] J.E. Garay, S.C. Glade, P. Asoka-Kumar, U. Anselmi-Tamburini, Z.A. Munir, J. Appl. Phys. 99 (2006) 024313.
[20] A.P. Druzhkov, B.A. Gizhevskii, V.L. Arbuzov, E.A. Kozlov, K.V. Shalnov, S.V. Naumov, D.A. Perminov, J. Phys. - Condens. Matter 14 (2002) 7981–7990.
[21] Y. Yagi, S. Hirano, Y. Ujihira, M. Miyayama, J. Mater. Sci. Lett. 18 (1999) 205–207.
[22] A.M. Massoud, R. Krause-Rehberg, H.T. Langhammer, J. Gebauer, M. Mohsen, Positron annihilation —ICPA12, Mat. Sci. Forum 363–365 (2001) 144–146.
[23] C.H. Shek, J.K.L. Lai, G.M. Lin, J. Phys. Chem. Solids 60 (1999) 189–193.
[24] X. Guo, J. Mater. Sci. Lett. 15 (1996) 2017–2019.
[25] P. Parente, G. Ferro, A. Tucci, L. Esposito, G. Timellini, Int. J. Mater. Prod. Technol. 35 (2009) 311–323.
[26] Kröger, The Chemistry of Imperfect Crystals, North Holland, Amsterdam, 1974.
[27] V. Butler, C.R.A. Catlow, B.E.F. Fender, Solid State Ionics 5 (1981) 539–542.
[28] E.C. Subbarao, H.S. Maiti, Solid State Ionics 11 (1984) 317–338.
[29] R. Birringer, Mater. Sci. Eng. A - Struct. Mater. Properties Microstruct. Process. 117 (1989) 33–43.
[30] X. Guo, Z.L. Zhang, Acta Mater. 51 (2003) 2539–2547.
[31] I.-W. Chen, X.H. Wang, Nature 404 (2000) 168–171.
[32] M. Mendelson, J. Am. Ceram. Soc. 52 (1969) 443–446.
[33] P. Kirkegaard, M. Eldrup, Comput. Phys. Comm. 3 (1972) 240–255.
[34] I. Gonzalo-Juan, Química Inorgánica, Universidad Autónoma de Madrid, Madrid, 2010, pp. 139–145.
[35] P. Garcia, B. Ferrari, R. Moreno, A.J. Sánchez-Herencia, M.T. Colomer, J. Eur. Ceram. Soc. 27 (2007) 4241–4244.
[36] C. Laberty-Robert, F. Ansart, C. Deloget, M. Gaudon, A. Rousset, Ceram. Int. 29 (2003) 151–158.
[37] I. Valov, C. Korte, R.A. De Souza, M. Martin, J. Janek, Electrochem. Solid State Lett. 9 (2006) F23–F26.
[38] I. Valov, J. Janek, Solid State Ionics 177 (2006) 1619–1624.
[39] A. Ovenston, Solid State Ionics 58 (1992) 221–229.
[40] J.F. Bartolomé, I. Montero, M. Díaz, S. López-Esteban, J.S. Moya, S. Deville, L. Gremillard, J. Chevalier, G. Fantozzi, J. Am. Ceram. Soc. 87 (2004) 2282–2285.
[41] S. Fabris, A.T. Paxton, M.W. Finnis, Acta Mater. 50 (2002) 5171–5178.
[42] M. Kilo, M.A. Taylor, C. Argirusis, G. Borchardt, M. Lerch, O. Kaitasov, B. Lesage, Phys. Chem. Chem. Phys. 6 (2004) 3645–3649.
[43] V.M. Orera, R.I. Merino, Y. Chen, R. Cases, P.J. Alonso, Phys. Rev. B 42 (1990) 9782–9789.
[44] B. Savoini, J.E.M. Santiuste, R. Gonzalez, Y. Chen, J. Lumines. 72–4 (1997) 714–715.
[45] S. Fabris, C. Elsasser, Acta Mater. 51 (2003) 71–86.
[46] X.L. Zhe, B. Li, S.H. Zhang, T.M. Wang, Phys. Status Solidi A 137 (1993) K9–K12.